Research Article Vol. 32, No. 5 / 26 Feb 2024 / Optics Express 7720
Optics EXPRESS

Three stage HCF fabrication technique for high yield, broadband UV-visible fibers

GREGORY JACKSON,[1,*] GREGORY T. JASION,[1] THOMAS D. BRADLEY,[1,2] FRANCESCO POLETTI,[1] AND IAN A. DAVIDSON[1]

[1]Optoelectronics Research Centre, Zepler Institute, University of Southampton, SO17 1BJ, United Kingdom
[2]Now at High-Capacity Optical Transmission Laboratory, Eindhoven University of Technology, 5600 MB, Netherlands
[*]g.jackson@soton.ac.uk

Abstract: Hollow-core optical fibers can offer broadband, single mode guidance in the UV-visible-NIR wavelength range, with the potential for low-loss, solarization-free operation, making them desirable and potentially disruptive for a wide range of applications. To achieve this requires the fabrication of fibers with <300 nm anti-resonant membranes, which is technically challenging. Here we investigate the underlying fluid dynamics of the fiber fabrication process and demonstrate a new three-stage fabrication approach, capable of delivering long (~ 350 m) lengths of fiber with the desired thin-membranes.

1. Introduction

Fused silica is the material of choice for optical fiber manufacture across a broad wavelength range (~ 350 to 2500 nm) due to its technological maturity and optical properties [1,2]. Traditionally optical fibers have an all-glass construction with a solid higher refractive index core and a lower index cladding. To achieve single-mode operation, the size of the core is scaled with the wavelength, and thus UV and visible guiding solid-core fibers have relatively small cores (~ 2 to 5 μm), making coupling light into them more challenging. A small core also increasing the fiber's non-linearity and reduces its power-handling capacity. Solid-core fibers also have limited single-mode bandwidth in the UV-visible (typically specified as 100 to 300 nm) meaning multiple fibers are needed to achieve guidance across the visible (400 to 800 nm) wavelength range. Moreover, the UV absorption edge of fused silica limits its use to >350 nm, with exposure to UV (<400 nm) light also leading to solarization, where the UV light causes the formation of permanent defects in the glass that reduce its transparency [3].

Although these issues have not stopped solid-core fibers use in the UV-visible wavelength range, fibers with larger cores, lower non-linearity, flatter dispersion, better power handling, and greater bandwidth capable of single-mode UV-visible guidance would be ideal for a range of applications including quantum computing [4–7], ultra-fast pulse delivery [8–10], non-linear light generation [11], non-linear microscopy [12–14], gas sensing [15], and high value manufacturing [16,17]. This need is particularly acute when it comes to <300 nm single-mode guidance, as presently there are limited options available to flexibly deliver these wavelengths [18]. Continuous broadband guidance (and low dispersion) is also of particular importance when working with ultra-fast pulses, if their ultra-short duration is to be maintained.

Hollow core fibers (HCFs) guide light in a gas- or vacuum-filled hollow core and are hence an ideal solution as they offer all of the desired properties [19], and are nearly immune to solarization [3,20,21]. Although multiple methods can be used to confine light within a hollow-core [19,22] this work focuses on anti-resonant HCFs where a single-ring of non-contacting cladding capillaries

#507703 https://doi.org/10.1364/OE.507703
Journal © 2024 Received 13 Oct 2023; revised 6 Jan 2024; accepted 12 Jan 2024; published 20 Feb 2024

Optics EXPRESS

are used to achieve this (fibers sometimes termed tubular, revolver, or negative-curvature). More advanced versions of this design are termed nested anti-resonant nodeless fibers (NANF), or conjoined fibers, where an extra membrane is added to reduce their optical loss [19,23]. The guidance mechanism in all these fibers results in minimal overlap between the guided light and the silica cladding material, hence the solarization immunity.

Anti-resonant, hollow-core fibers (AR-HCFs) offer multiple low-loss transmission windows bounded by high loss resonant regions, which can be calculated via the ARROW model [19,22]:

$$\lambda_m = \frac{2t}{m}\sqrt{n_2^2 - n_1^2} \qquad m = 1, 2, 3 \tag{1}$$

where λ_m is the m-th resonant wavelength, m is the resonance order, t is the cladding capillary membrane thickness, n_2 is the glass refractive index, and n_1 is the gas refractive index (typically ~ 1 for air at standard atmospheric pressure).

These transmission windows exhibit decreasing bandwidth with increasing resonance order, thus while fibers with thicker capillary membranes will guide UV-visible light in their higher order transmission windows, the presence of resonances between these windows reduces the potential bandwidth [24–27], and in turn, potentially limits their use. Thus, despite the thicker membranes making the structure more easily controlled during the fiber draw (as will be discussed later), and hence potentially improving the fibers optical performance, these higher order window UV-visible guiding fibers offer at most 300 to 400 nm of continuous guidance, equivalent to ~0.7-0.8 octaves [24,25].

In the case of the lowest order transmission window the lack of resonance on the long wavelength edge results in greater bandwidth, with 1.6 octaves demonstrated in the NIR [28] and ~1.7 (through a short length) in the visible [29], offering the possibility of true broadband UV-visible (potentially from #250 to beyond 750 nm) guidance. But to make this a reality requires the fabrication of fibers with thin (<300 nm) capillary membranes, which is technically challenging due to an increased likelihood of capillary contact during the fiber draw process, harming their optical performance. A number of post-processing fabrication techniques exist to reduce the membrane thickness of drawn fibers [30–32] but come with their own limitations, often in terms of fiber length.

In this work we present a new fabrication approach that allows the production of long lengths (~ 350 m thus far, potentially >2 km as described) of fiber with thin (<300 nm) capillary membranes. Further we use numerical modelling to explore the fluid dynamics of the draw process and limitations on the fabrication of AR- HCFs and explain the benefits of the proposed process. Finally, we demonstrate a series of example fibers with (<300 nm) membranes capable of broadband UV-visible guidance.

2. AR-HCF fiber drawing model and draw dynamics

Figure 1(A) shows a schematic of the geometry of a AR-HCF, where g is the inter-capillary gap size, D is the capillary outer radius, ϕ is the core diameter, D_j is outer diameter, and d_j is the inner diameter. AR-HCFs are commonly fabricated using a 2-stage stack and draw technique [33], where a macroscopic (few cm diameter) "stack" is constructed by stacking capillaries within an outer tube, which is then fused and drawn to millimeter sized canes. These canes are then inserted into a larger jacket tube and drawn to fiber. During the draw the core and capillaries are pressurised to achieve the desired structure, as will discussed in more detail later.

When drawing optical fibers using this approach, the reduction in diameter from preform to fiber leads to complex dynamics, and results in a structure termed a "neckdown". Fiber drawing models, based on the fluid dynamics of fused silica, provide a method to understand these dynamics and hence the draw process. We use an analytical steady-state model for basic

Optics EXPRESS

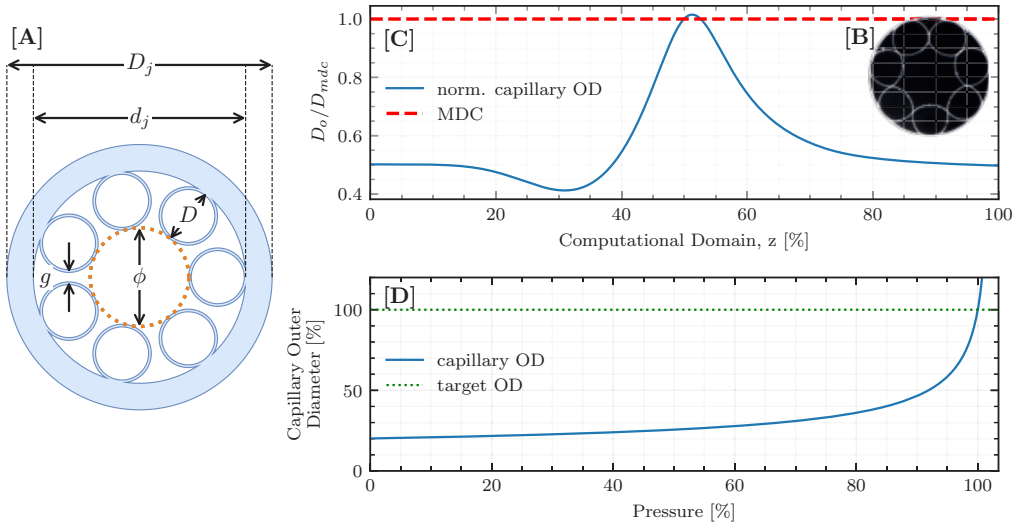

Fig. 1. A) Schematic of the geometry of a 7-capillary AR-HCF. B) Radial profile of the capillaries normalised to the mid-drawn contact (MDC) radius along z. The dashed red line is the radius at which MDC occurs. The inset shows an example microscope image of a fiber with MDC. C) Capillary outer diameter as a function of applied pressure. Target outer diameter indicated by the dotted green line.

capillaries derived from the Navier-Stokes equations [34], which provides a 1-dimensional solution for the longitudinal evolution of the outer and inner radius.

The neckdown profile is then found by:

$$\rho(R^2 - r^2)\left(v\frac{dv}{dz} - g\right) = \frac{d}{dz}(3\mu(T)(R^2 - r^2)\frac{dv}{dz} + \gamma(R + r) \tag{2}$$

$$\frac{dR^2v}{dz} = \frac{dr^2v}{dz} = \frac{pR^2r^2 - \gamma Rr(R + r)}{\mu(T)(R^2 - r^2)} \tag{3}$$

$$\frac{R^2 - r^2}{2}\left[\rho c_p(T)v\frac{dT}{dz} - \sigma\alpha(T_a^4 - T^4)\right] = RN(T_a - T) \tag{4}$$

where $R = R(z)$ is the outer radius, $r = r(z)$ is the inner radius, $v = v(z)$ is glass velocity, ρ is the glass density (2200 kg/m^3 for silica), γ is the surface tension (0.3 N/m for silica), $\sigma = 5.67 \times 10^{-8}$ W/m^{2}K^4 is the Stefan-Boltzmann constant, g is the acceleration from gravity, $\alpha = 0.885\,\mathrm{m}^{-1}$ is a factor associated with emissivity, $N = 100$ W/m^{2}K is the heat transfer coefficient, p is the applied pressure (assumed constant throughout z), T is the glass temperature, $T_a = T_a(z)$ is the furnace temperature, $\mu(T)$[Pa s] is the viscosity, and $c_p(T)$[J kg^{-1} K] is the specific heat.

Eqaution (2) and (4) form a coupled system of differential equations, with the preform geometry defining the boundary conditions at $z = 0$. In our model the values of strain rate, pressure, and furnace temperature which result in the correct fiber geometry are found numerically via a goalseeking algorithm. The model is extended to AR-HCFs by first solving the jacket tube as described, then using its axial solution to solve the outer and inner radii of the internal capillaries [35]. The combined solutions provide the required fabrication parameters which satisfy the target geometry, such as furnace temperature, core pressure, and capillary pressure.

Optics EXPRESS

2.1. Mid-draw contact and pressure sensitivity

Surface tension exerts a contracting pressure inversely proportional to capillary radius during the fiber draw, as given by the Young-Laplace equation $p_\gamma = -\gamma/r$. The interplay of applied pressure and surface tension leads to the complex micro-structure dynamics encountered. At the start of the neckdown region the capillaries are large and gas pressure dominates. However, as the preform approaches fiber scale, a cross-over point is reached and surface tension starts to dominate and the capillaries contract. Therefore, if the target fiber geometry is to be reached, this unavoidable contraction phase must be compensated for by over expanding the capillaries during the pressure dominated phase. In the limiting case, the capillaries will need to be expanded such that contact occurs, an undesirable effect termed mid-draw contact (MDC), resulting in glass nodes which introduce additional high-loss regions to the fibers optical transmission, affecting its loss [22,35]. Figure 1(B) shows a microscope image of a fiber which has experienced MDC.

Due to the practicalities of the fiber drawing process (fabrication tolerances, pressure variation and drift, etc.), a buffer pressure to the predicted MDC point is required to ensure MDC does not occur, termed the *MDC pressure buffer* here and defined as $\Delta p_b = p_{mdc} - p_{to}$, where p_{mdc} is the minimum pressure which results in MDC, and p_{to} is the pressure required to reach the target geometry. A negative or zero value of Δp_b indicates that the target structure cannot be reached without experiencing MDC. Using the draw model outlined in the previous section, it is possible to calculate the outer capillary radius throughout the neckdown. The capillary radius at which MDC occurs can be calculated from simple geometry. It is then a matter of stepping through the neckdown solution to see if the predicted capillary size is sufficient for MDC to have occurred. Figure 1(C) presents an example neckdown simulation demonstrating a fiber draw where MDC occurs. The pressure and surface tension dominated phases are also clearly visible.

When targeting thinner capillaries, the draw yield per meter of preform (hereafter termed *draw yield*) will increase. The resulting increase to the strain rate, dv/dz, must be balanced by increasing the furnace temperature if the target draw tension is to be maintained. Increasing the furnace temperature decreases the glass' viscosity, making the capillaries more sensitive to the applied pressure at the start of the neckdown, increasing the likelihood of MDC. This rapidly becomes the primary limiting factor when targeting fibers with thin (<300 nm) membranes if draw tension is not increased above the original target; as will be discussed later.

Another dynamic to consider is the capillary's sensitivity to applied pressure as its diameter is increased. This sensitivity will change as the capillary is expanded as its thickness will be reduced, and hence the relationship is non-linear. While this is not a limiting factor in itself, if the sensitivity becomes too high it can be problematic in terms of realising a specific capillary diameter or avoiding MDC due to practical issues, such as the pressure controller resolution. Pressure sensitivity can be determined by using the Fitt model to simulate capillary expansion with pressure and then calculating the slope at a desired outer diameter or pressure. An example is shown in Fig. 1(D). A lower sensitivity is also desirable from the perspective of producing uniform fiber.

3. Fabrication dynamics for thin-membraned fibers

There are principally two routes to avoiding MDC during a fiber draw - increasing the draw tension (making the glass stiffer and hence less sensitive to pressure) or reducing the size of the preform and hence the strain rate, dv/dz, as detailed above [36]. Both approaches potentially result in a reduction in the fiber yield, through a reduction in starting material in the case of a smaller preform, and fiber breakage in the case of increased tension, which is undesirable. However, as fiber breakage is stochastic in nature, has other downsides, and is easily understood, it will not be considered here.

The reduction in draw yield due to cane scaling can also be avoided by simply scaling its volume at the same rate as that of the desired fiber, and this is the approach that will be presented

Optics EXPRESS

here. This has the additional benefits that the resultant strain rate will also remain constant meaning the glass viscosity does not need to be reduced to avoid MDC, and the capillary pressure sensitivity should be reduced, both of which are obviously desirable.

Using the fiber drawing model in 2, the relationship between draw yield and cane outer diameter to fiber capillary thickness at the limit of MDC for a 7-capillary AR-HCF can be explored. While there have been fibers with a range of different capillary numbers [3,19–21,23–32], a 7-capillary geometry was chosen for its good compromise between bend loss and high-order mode suppression [8]. However, the analysis report is fully general and could thus be scaled to other designs, including nested/conjoined tube fibers.

The fiber geometry used in the simulations shown in Fig. 2 were based on the fiber capillary thickness, t, with all parameters and corresponding formulae shown in Table 1, and varying the thickness over the range 150 to 1000 nm in steps of 50 nm. The cane support tube and capillaries were set to a fixed ratio of inner to outer diameter of 0.86, and then for each target fiber scaled using mass conservation such that a chosen fiber draw yield is achieved. For practical reasons a small gap between the outside of the cane and inside of the jacket tube is necessary and for the simulations present here this is set to 0.5 mm. The jacket outer diameter is determined by goalseeking such that the target fiber outer diameter is met. This process was repeated for various draw yields. The simulations were set to a fixed draw stress of 250 MPa. While this is a high value for solid core fibers, this is inline with those typically used for HCFs [37]. It also offers a good compromise between the risk of fiber breaks during the draw and enables fair comparison.

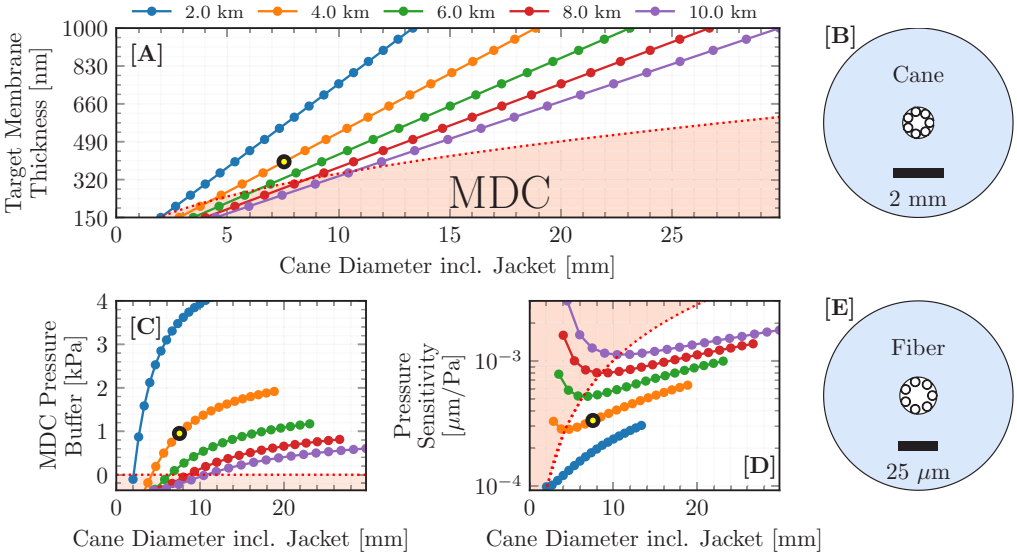

Fig. 2. Simulations of fibers maintaining a specific draw yield, each line represents a draw yield. The shaded red regions represent $\Delta p_b \leqslant 0$, the MDC zone. A) Map of the target membrane thickness and cane outer diameter. Yellow dot indicates the cane-fiber combination displayed in Fig. 2(B) and (E). B) Example schematic of a cane. C) Effect of draw yield and cane outer diameter on MDC pressure buffer. D) Sensitivity of draw yield and cane outer diameter on applied pressure. E) Example schematic of a fiber.

Each fiber and cane combination simulated is marked by a dot in Fig. 2(A), with each draw yield being represented by a different colour. In each subplot, the dotted red line and shaded region represent cane and fiber combinations with $\Delta p_b \leqslant 0$, the MDC zone. As expected, decreasing the draw yield (cane size) has the effect of reducing the minimum membrane thickness attainable without MDC, while also increasing the MDC pressure buffer and decreasing the

Optics EXPRESS

Table 1. Fiber geometrical parameters and their corresponding equations, used to build geometrically similar fibers scaled on the membrane thickness, *t*. Corresponding cane calculated using conservation of mass.

Description	Parameter	Equation
Membrane Thickness [nm]	t	t
Core Diameter [μm]	ϕ	$30t$
Inter-capillary Gap	δ	0.15ϕ
Capillary Outer Diameter	R_c	$\frac{\delta-\phi\sin(\frac{\pi}{N})}{\sin(\frac{\pi}{N})-1}$
Fiber Outer Diameter	R_j	10ϕ
Fiber Inner Diameter	r_j	$2R+\phi$

pressure sensitivity. This is most clearly seen when comparing the intersection of the 10 km and 1 km yield lines with the MDC zone, with the 10 km yield resulting in a minimum thickness of 478 nm (and a pressure sensitivity of 0.0047 μm/Pa), while the 1 km draw has a minimum thickness of 142 nm (and pressure sensitivity of 0.00014 μm/Pa) for the chosen fiber geometry.

Another way to interpret the data presented is as follows: To achieve continuous guidance of the whole visible spectrum range (400 to 800 nm), a fiber with a capillary membrane thicknesses of less than ~ 185 nm is needed, and hence a cane size of <2.04 mm would be required to avoid MDC. The exact cane size necessary to achieve differing fiber geometries will obviously be different but generally to produce a AR-HCF with thin membranes, and reasonable loss, a small diameter (<2 mm) cane is likely necessary, which may be problematic, as it will be both difficult to handle and may make pressurisation challenging.

Recently an alternative approach to HCF fabrication has been reported where self-pressurisation (induced by sealing of areas of the fiber preform) is used instead of active pressurisation [38]. Although practically this approach is different to the one outlined here, the underlying fluid-dynamics are the same, and hence it will suffer from the same limitations. However, the lack of active pressurisation may make the use of smaller canes more practical, even if these (and the resultant fiber preform) will still be difficult to handle. Further, self-pressurisation is inherently less controlled making the collection of long lengths of uniform fiber difficult.

4. Three stage HCF fabrication technique

A potential route to achieving all the benefits of a smaller diameter cane, whilst avoiding the associated problems, is to introduce an additional stage to the 2-stage stack and draw fabrication process described earlier. In this additional stage the jacketed fiber preform is drawn to an intermediate 2nd cane stage, termed CS2 (with the first cane now being termed CS1), see Fig. 3 [39]. As such the fabrication process will then consists of: 1) build a stack and draw it to an initial CS1 cane, 2) jacket the cane and draw it to a 2nd stage, CS2, cane, and 3) draw CS2 to fiber. This is accomplished by passing the preform through the fiber drawing tower furnace twice, but at different speeds, and has the major benefit of preserving the neckdown between the cane stages, allowing the smaller diameter cane to be pressurised through the larger one. A contour map of draw stress, CS2 outer diameter, and MDC pressure buffer for an example fiber is shown in Fig. 4, with a schematic of the target fiber inset. To ensure the fiber is achievable a minimum MDC pressure buffer of $\Delta p_b = 0.03$ kPa, as indicated by the dashed green line, was chosen. Based on the plot and pressure buffer requirement, a range of suitable CS2 diameters and draw stress values can be identified. In this process either draw stress or CS2 diameter (fiber yield) can be chosen as a free parameter, and used to tune the details of the fiber draw. Since draw stress also affects the total pressure requirement to achieve the desired structure, it was selected as the free-parameter in this case and used to tune the pressure; as shown by the overlaid

Optics EXPRESS

dotted lines. Based on this contour map, a suitable fabrication window can be identified that will allow the desired fibre geometry to be fabricated given a specific total pressure or fibre yield (or potentially draw stress) requirement.

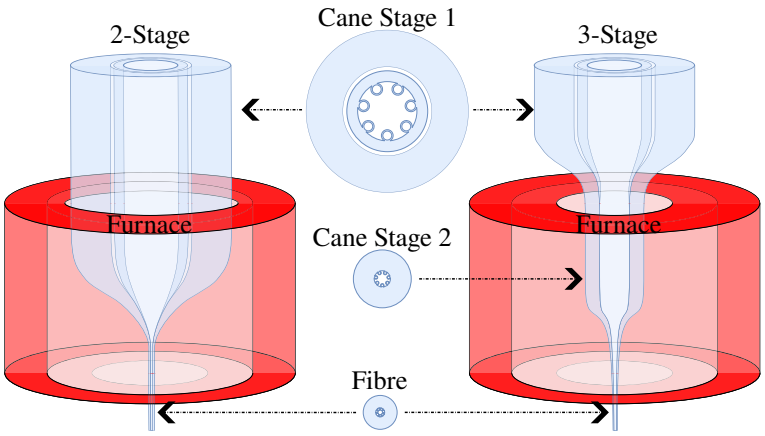

Fig. 3. Comparison of a conventional fibre draw of a 2-stage method with the proposed 3-stage technique. Left) The 2-stage technique with a single neckdown. Right) The 3-stage, with two neckdowns. Red cylinder represents the furnace. Note scale is exaggerated for clarity.

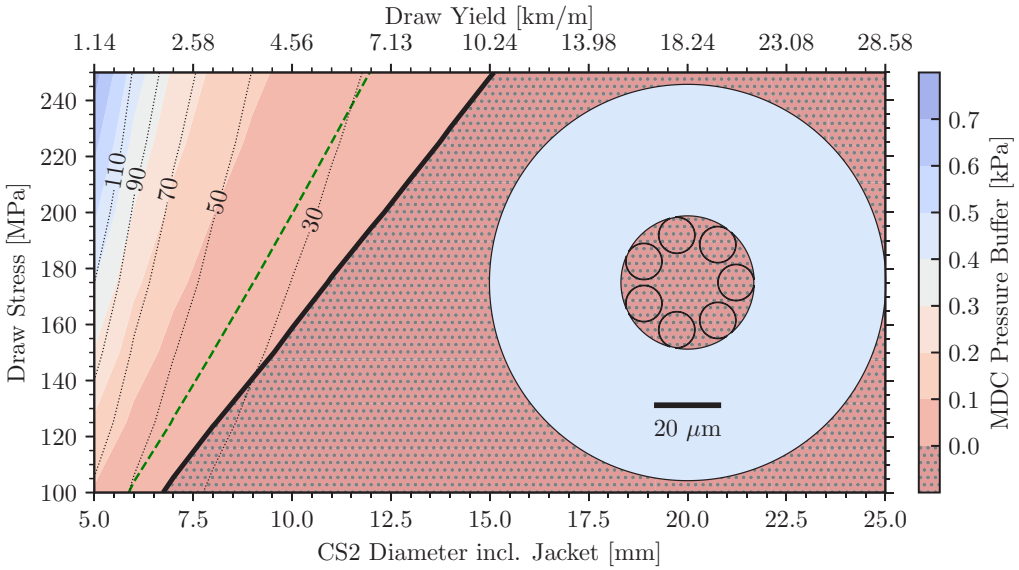

Fig. 4. The effect of cane outer diameter and draw stress on both Δp_b and pressure requirements when targeting a fixed fiber design. The shaded contours represent the MDC pressure buffer in steps of 0.1 kPa. Dotted lines show the required pressure (core + capillary). The solid black line represents $\Delta p_b = 0$ (fibers are not achievable to its right). The dashed green line shows $\Delta p_b = 0.03$ kPa.

Optics EXPRESS

5. Experimental results

A series of 7-capillary fibers were drawn via the described 3-stage process. This fiber design was chosen as it has been shown to offer the best compromise between loss, bend-loss, and higher-order mode suppression for a single-cladding ring geometry [8,19]. Based on the targeted fiber geometries a series of contour plots, like those in Fig. 4, were generated to allow suitable draw conditions to be selected. These resulted in CS2 diameters of ~ 5.9 to 6.5 mm and draw stresses from ~ 110170 MPa being selected; resulting in theoretical maximum yields of ~ 1.5 to 3 km per meter of CS2.

In these draws several shorter bands were collected. The transmission of three representative bands is shown in Fig. 5. These measurements were made using a Energetiq EQ-99X laser-driven light source (likely absorption limited to ~ 280 to 2100 nm), and a Teledyne-Princeton Instruments HRS-500 and PIXIS-256 spectrometer (capable of measuring 200 to ~ 1100 nm).

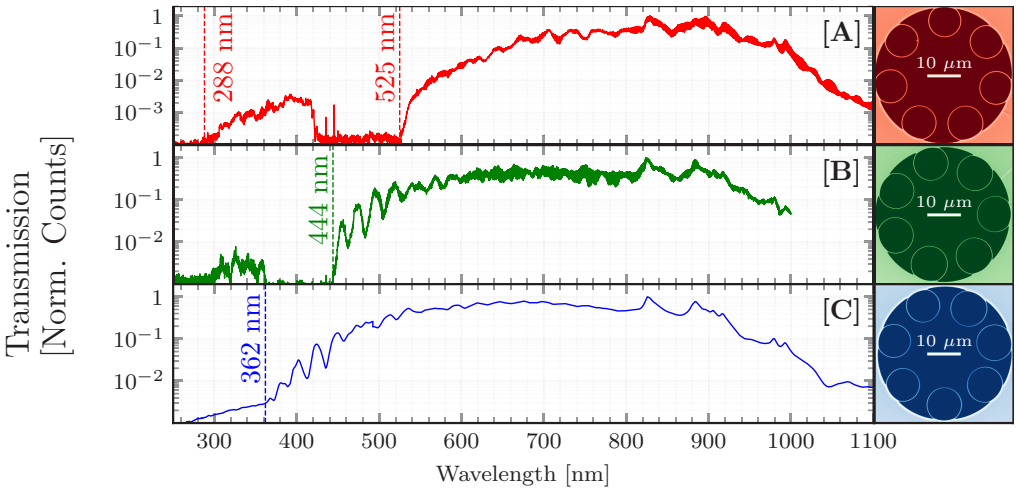

Fig. 5. Left) Transmission profiles between 250 nm to 1100 nm for AR-HCFs A, B, and C fabricated with 3-stage fabrication technique. Transmission spectra measured at fibers lengths 1.5 m, 5.2 m, and 6 m respectively. Right) A,B, and C Scanning electron microscope images.

Based on the position of the short-wavelength edge of the transmission windows in these fibers, as indicated in the figure, and the ARROW model, Eq. (1) [22], their membrane thicknesses are estimated to be 254(±8), 207, and 167 nm for A to C respectively. These thickness estimates are in reasonable agreement with those obtained from the included SEMs for fibers A and B. However, the SEM of fiber C predicts a thickness of <130 nm. We attribute this discrepancy to how the SEMs electron beam interacts with the thin membranes and believe the (thicker) figure obtained from the transmission is likely to be more accurate.

Fibers B and C guide from 444 and 362 nm to beyond 1000 and 1100 nm respectively in their lowest order (1^{st}) anti-resonant (AR) window, and hence demonstrate continuous guide of the entire (or nearly entire) visible (400 to 800 nm) wavelength range, as well as part of the NIR. In the case of fiber C, this represents >1.6 octaves of bandwidth. Due to equipment limitations and strong atmospheric absorption below a wavelength of 200 nm it was not possible to measure fiber C's 2^{nd} AR transmission window or the short wavelength edge of fiber B's 2^{nd} window, but based on the membrane thicknesses determined, these fibers are predicted to guide 190 to 290 nm and 231 to 365 nm respectively, also making them highly interesting for UV applications.

Optics EXPRESS

Figure 6 [A] and [C] show microscope images of the start and end of the 346 m band associated with the fiber reported in Fig. 5 [C]. These images show some structural evolution along the band has occurred; primarily the core size has increased by ~ 0.7*um* (3.5%) due to a mixture of the fiber inner diameter increasing (40.2 to 40.5 µ m) and the cladding capillary diameter reducing (by ~ 0.1 µm). This sort of evolution is sometimes seen during fiber fabrication, particularly towards the end of a fiber draw, as was the case with this band.

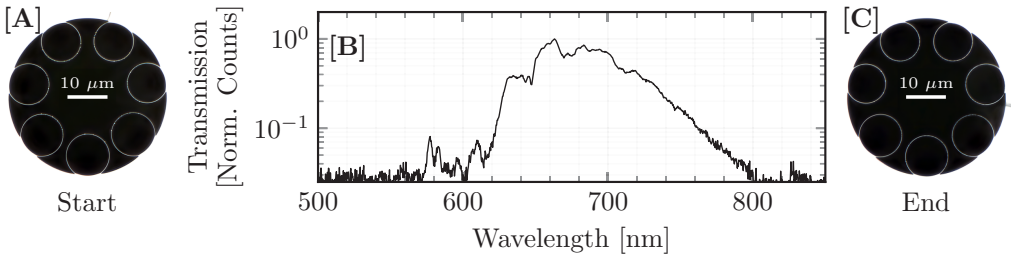

Fig. 6. [A] Microscope image of start of (346 m) band associated with the fiber reported in Fig. 5 [C]. [B] Transmission through full 346 m band. [C] Microscope image of the end of band.

Figure 6 [B] shows a transmission measurement of the full 346 m band, measured using the same setup as the measurements in Fig. 5. This full band guides from ~ 600 to 800 nm which, while considerably narrower than Fig. 5 [C], represents ~ 0.4 octaves of bandwidth, similar to the specified single-mode bandwidth of commercial visible (solid-core) fibers. This bandwidth narrowing is likely due to a combination of the underlying loss profile of the fiber and the structural evolution seen along the fibers length. Both of these will be addressed in future draws as this process is further refined. As the measurements shown in Fig. 5 [C] and Fig. 6 [C] were made under different conditions they are unsuitable for loss determination, but a recent preliminary loss measurement suggests the loss of this fiber is <100 dB/km from ~ 500 to 800 nm [40]. Full characterisation of all the fibers shown in Fig. 5 is currently underway.

The fibers shown in Figs. 5 and 6 demonstrate the benefits of the 3-stage draw process as it would be extremely difficult to achieve the same geometries (using the same preform design) via the traditional 2-stage process as, for example, draw stress of 360, 511, and 753 MPa would be required (if a $\Delta p_b \geqslant 0.003$ kPa, sufficient to avoid MDC, is to be maintained) for fiber A to C respectively, making fiber breakage during drawing highly likely. The 346 m length reported in Fig. 6 also represents a >3x improvement in fiber yield compared to the current state of the art for AR-HCFs with <200 nm membranes [3,29]. As the theoretical maximum yield of the preform design currently being used is >2 km, it suggests this process may already be suitable for commercial fabrication.

6. Conclusion

In this paper we have explored the fluid dynamic limitations imposed upon hollow-core fiber design by the fabrication process. Based on this analysis a viable new route to the fabrication of anti-resonant hollow-core fibers with thin (<300 nm) membranes in lengths exceeding several hundred metres per draw has been demonstrated. Using this method, a series of UV-visible-NIR guiding fibers have been demonstrated including one, with ~ 167 nm membranes, capable of guiding light from ~ 360 to >1100 nm, >1.6 octaves of bandwidth. This work expands what is possible in terms of anti-resonant hollow-core fiber fabrication and offers a potential route to the commercial manufacture of hollow-core fibers suitable for broadband UV-visible guidance.

Funding. Engineering and Physical Sciences Research Council (EP/P030181/1).

Optics EXPRESS

Disclosures. The authors declare no conflicts of interest.

Data availability. All data supporting this study are openly available from the University of Southampton Repository [41].

References

1. Y. Tamura, H. Sakuma, K. Morita, *et al.*, "The first 0.14-db/km loss optical fiber and its impact on submarine transmission," J. Lightwave Technol. **36**(1), 44–49 (2018).
2. C. Kurkjian, J. Krause, and M. Matthewson, "Strength and fatigue of silica optical fibers," J. Lightwave Technol. **7**(9), 1360–1370 (1989).
3. F. Yu, M. Cann, A. Brunton, *et al.*, "Single-mode solarization-free hollow-core fiber for ultraviolet pulse delivery," Opt. Express **26**(8), 10879–10887 (2018).
4. C. D. Bruzewicz, J. Chiaverini, R. McConnell, *et al.*, "Trapped-ion quantum computing: Progress and challenges," Appl. Phys. Rev. **6**(2), 021314 (2019).
5. T. D. Ladd, F. Jelezko, R. Laflamme, *et al.*, "Quantum computers," Nature **464**(7285), 45–53 (2010).
6. C. Zhang, F. Pokorny, W. Li, *et al.*, "Submicrosecond entangling gate between trapped ions via rydberg interaction," Nature **580**(7803), 345–349 (2020).
7. P. Hrmo, B. Wilhelm, L. Gerster, *et al.*, "Native qudit entanglement in a trapped ion quantum processor," Nat. Commun. **14**(1), 2242 (2023).
8. M. Michieletto, J. K. Lyngsø, C. Jakobsen, *et al.*, "Hollow-core fibers for high power pulse delivery," Opt. Express **24**(7), 7103–7119 (2016).
9. S. Eilzer and B. Wedel, "Hollow core optical fibers for industrial ultra short pulse laser beam delivery applications," Fibers **6**(4), 80 (2018).
10. B. Debord, M. Alharbi, L. Vincetti, *et al.*, "Multi-meter fiber-delivery and pulse self-compression of milli-joule femtosecond laser and fiber-aided laser-micromachining," Opt. Express **22**(9), 10735–10746 (2014).
11. A. Lekosiotis, F. Belli, C. Brahms, *et al.*, "On-target delivery of intense ultrafast laser pulses through hollow-core anti-resonant fibers," arXiv, arXiv:2305.16911 (2023).
12. D. Kim, H. Choi, S. Yazdanfar, *et al.*, "Ultrafast optical pulse delivery with fibers for nonlinear microscopy," Microsc. Res. Tech. **71**(12), 887–896 (2008).
13. V. V. Yakovlev, "Advanced instrumentation for non-linear raman microscopy," J. Raman Spectrosc. **34**(12), 957–964 (2003).
14. A. Kudlinski, A. Cassez, O. Vanvincq, *et al.*, "Double clad tubular anti-resonant hollow core fiber for nonlinear microendoscopy," Opt. Express **28**(10), 15062–15070 (2020).
15. T. W. Kelly, I. A. Davidson, C. Warren, *et al.*, "Sub-ppm gas phase raman spectroscopy in an anti-resonant hollow core fiber," Opt. Express **30**(24), 43317–43329 (2022).
16. D. Y. You, X. D. Gao, and S. Katayama, "Review of laser welding monitoring," Sci. Technol. Weld. Joining **19**(3), 181–201 (2014).
17. S. Engler, R. Ramsayer, and R. Poprawe, "Process studies on laser welding of copper with brilliant green and infrared lasers," Phys. Procedia **12**, 339–346 (2011).
18. K.-F. Klein, C. P. Gonschior, D. Beer, *et al.*, "Silica-based UV-fibers for DUV applications: current status," in *Micro-structured and Specialty Optical Fibres II*, vol. 8775 K. Kalli, J. Kanka, and A. Mendez, eds., International Society for Optics and Photonics (SPIE, 2013), p. 87750B.
19. F. Poletti, "Nested antiresonant nodeless hollow core fiber," Opt. Express **22**(20), 23807–23828 (2014).
20. F. Gebert, M. H. Frosz, T. Weiss, *et al.*, "Damage-free single-mode transmission of deep-uv light in hollow-core pcf," Opt. Express **22**(13), 15388–15396 (2014).
21. D. Dorer, M. H. Frosz, S. Haze, *et al.*, "Hollow-core fiber for single-mode, low loss transmission of broadband uv light," arXiv, arXiv:2304.14779 (2023).
22. N. M. Litchinitser, A. K. Abeeluck, C. Headley, *et al.*, "Antiresonant reflecting photonic crystal optical waveguides," Opt. Lett. **27**(18), 1592–1594 (2002).
23. S.-F. Gao, Y.-Y. Wang, W. Ding, *et al.*, "Hollow-core conjoined-tube negative-curvature fibre with ultralow loss," Nat. Commun. **9**(1), 2828 (2018).
24. I. Davidson, M. C. Partridge, J. Hayes, *et al.*, "Tubular anti-resonant hollow core fiber for visible raman spectroscopy," in *Sixth International Workshop on Specialty Optical Fibers and Their Applications (WSOF 2019): Conference Digest*, vol. 11206 J. Ballato and L. Dong, eds. (SPIE, 2019).
25. J. H. Osório, F. Amrani, F. Delahaye, *et al.*, "Hollow-core fibers with reduced surface roughness and ultralow loss in the short-wavelength range," Nat. Commun. **14**(1), 1146 (2023).
26. H. Sakr, Y. Chen, G. T. Jasion, *et al.*, "Hollow core optical fibres with comparable attenuation to silica fibres between 600 and 1100 nm," Nat. Commun. **11**(1), 6030 (2020).
27. J. Boullet, F. Gérôme, F. Leroi, *et al.*, "Record power transmission of intense 343 nm UV radiation in a singlemode inhibiting coupling hollow-core fiber exceeding 20W of 10-ns pulses," in *Europhoton*, (Hannover, Germany, 2022), pp. WED-FWD-3.4.
28. J. R. Hayes, S. R. Sandoghchi, T. D. Bradley, *et al.*, "Antiresonant hollow core fiber with an octave spanning bandwidth for short haul data communications," J. Lightwave Technol. **35**(3), 437–442 (2017).

Optics EXPRESS

29. S. F. Gao, Y. Y. Wang, X. L. Liu, *et al.*, "Nodeless hollow-core fiber for the visible spectral range," Opt. Lett. **42**(1), 61–64 (2017).
30. R. Pennetta, M. T. Enders, M. H. Frosz, *et al.*, "Fabrication and non-destructive characterization of tapered single-ring hollow-core photonic crystal fiber," APL Photonics **4**(5), 056105 (2019).
31. W. Gilliam, B. T. Fleming, D. Vorobiev, *et al.*, "Far-ultraviolet optical fibers for instrumentation in the sub-200 nm regime," in *UV/Optical/IR Space Telescopes and Instruments: Innovative Technologies and Concepts X*, vol. 11819 A. A. Barto, J. B. Breckinridge, and H. P. Stahl, eds., International Society for Optics and Photonics (SPIE, 2021), p. 118190L.
32. V. T. Hoang, G. Stepniewski, R. Kasztelanic, *et al.*, "Enhancement of uv-visible transmission characteristics in wet-etched hollow core anti-resonant fibers," Opt. Express **29**(12), 18243–18262 (2021).
33. J. C. Knight, T. A. Birks, P. S. J. Russell, *et al.*, "All-silica single-mode optical fiber with photonic crystal cladding," Opt. Lett. **21**(19), 1547–1549 (1996).
34. A. Fitt, K. Furusawa, T. Monro, *et al.*, "The mathematical modelling of capillary drawing for holey fibre manufacture," J. Eng. Math. **43**(2/4), 201–227 (2002).
35. G. T. Jasion, J. R. Hayes, N. V. Wheeler, *et al.*, "Fabrication of tubular anti-resonant hollow core fibers: modelling, draw dynamics and process optimization," Opt. Express **27**(15), 20567–20582 (2019).
36. G. Jackson, T. D. Bradley, G. T. Jasion, *et al.*, "Exploring fabrication limits for uv guiding hollow core anti-resonant fiber," in *Frontiers in Optics + Laser Science 2021*, (Optica Publishing Group, 2021), p. FW1C.3.
37. M. Corrado, D. J. DiGiovanni, B. Mangan, *et al.*, "Hollow core optical fiber with controlled diameter hollow regions and method of making the same," (2021).
38. L. R. Murphy, S. Yerolatsitis, T. A. Birks, *et al.*, "Stack, seal, evacuate, draw: a method for drawing hollow-core fiber stacks under positive and negative pressure," Opt. Express **30**(21), 37303–37313 (2022).
39. G. Jackson, I. A. Davidson, T. D. Bradley, *et al.*, "Fabricating thin membraned anti-resonant hollow-core fibre for broadband uv-visible light guidance," in *Optica Advanced Photonics Congress 2022*, (Optica Publishing Group, 2022), p. SoTu1I.1.
40. I. A. Davidson, G. Jackson, T. Kelly, *et al.*, "Next generation uv-visible single-mode fibers," in *CLEO: Science and Innovations*, (Optica Publishing Group, 2023), p. STh3G.1
41. G. Jackson, G. T. Jasion, T. D. Bradley, *et al.*, Data for: "Three stage HCF fabrication technique for high yield, broadband UV-visible fibers", University of Southampton Repository, (2024) https://www.doi.org/10.5258/SOTON/D2954.